



Improving the Wear Properties of AISI4130 Steel Using Laser Surface Hardening Treatment

Meisam Bakhtiari¹ · Alireza Fayazi Khanigi² · Amirreza Farnia^{3,4}

Received: 29 September 2022 / Accepted: 12 December 2022 / Published online: 5 January 2023
© King Fahd University of Petroleum & Minerals 2023

Abstract

This study aimed to investigate the hardness of laser transformations on AISI4130 steel using high-power Nd:YAG pulsed laser technology. Beam scanning speed, focal distance, and peak power were used as available variables for the experiments. An optical microscope, scanning electron microscope, microhardness, and wear tests were performed to assess microstructural changes. In laser transformation hardening, at a maximum power of 3.5 kW, a frequency of 7 Hz, an out-of-focus distance of 10 mm, and a scanning speed of 5 mm/s, the maximum hardened depth and width were measured as 0.4 and 2 mm, respectively. The predominant microstructure in the heat-affected zone was mainly martensite and bainite, with a maximum hardness of 650 and 530 HV, respectively. At constant beam scan velocities, reduction in the focal point position relative to the sample surface was associated with increased depth of the hardened area. Hardened samples were subjected to a pin-on-disk wear test, and it was found that the coefficient of friction decreased from 0.77 for the base metal to 0.39 in the hardened samples. The wear surface of the hardened sample exhibited a combination of abrasive and adhesive wear. Therefore, optimal conditions are achieved by beam velocity and focal length. Laser paths with 20% lateral overlap were tested to expand the hardened areas and simulate the actual conditions of primary workpiece. Thermal cycles cause preheating in previously hardened areas and reduce the hardness of these areas in the range of 300 to 400 μm from the surface to 100 HV.

Keywords Laser surface hardening · Wear behavior · Surface transformation hardening · AISI4130 steel · Nd: YAG laser

1 Introduction

Regarding the surface improvement process of a material, especially steels, which are widely used in industry, it is possible to refer to common methods of heat treatment, including induction and flame heat treatment methods, which can be precisely processed with new techniques such as lasers [1]. Recently, laser technology has been used for various industrial applications such as laser cladding [2, 3], laser welding

[4–7], laser hardening [8], laser cutting [9], laser surface processing [10], and surface alloying [11, 12]. Compared to other hardening processes such as flame hardening and induction hardening, laser surface hardening has better compatibility with small components, greater precision, a smaller risk of distortion, and non-hardenable steels, like mild steels, can be surface hardened. In the country, in this process, the high initial and working cost is high and extra care is needed to avoid melting [13, 14]. Laser surface hardening is a desirable process for increasing the surface properties of a sample. While the desired material properties, such as toughness, remain unchanged, in contrast, the wear resistance, fatigue, and corrosion resistance of metals and their alloys are improved by this process [15, 16]. The desired hardness, and depth of it, can be changed by adjusting the laser parameters such as scanning speed, out-of-focus distance, power, etc. These parameters significantly affect the uniformity, microstructure, and chemical composition of hardened laser layers, but it is impossible to achieve precision and quality with conventional methods. The fundamental parameters that affect laser hardening include laser power, beam characteristics, speed,

✉ Alireza Fayazi Khanigi
alireza_fayazi@modares.ac.ir

¹ Faculty of Materials Science and Engineering, K.N. Toosi University of Technology, Tehran, Iran

² Department of Materials Science and Engineering, Tarbiat Modares University, Tehran, Iran

³ Department of Materials Engineering, Science and Research Branch, Islamic Azad University, Tehran, Iran

⁴ Department of Surface Engineering, Research and Development of Engineering Material Research Center, Science and Research Branch, Islamic Azad University, Tehran, Iran



and out-of-focus distance relative to the specimen surface. Beam power is one of the most critical parameters. The key beam properties in laser surface hardening (LSH) processes are: beam condition, stability, polarization, and beam shape (pulsed or continuous).

It can be noticed that as the scanning speed decreases, the laser energy radiates longer onto the surface of the workpiece. Therefore, the energy density increases, and the amount of hardness and depth of the hardened sample increases. Also, one of the most critical parameters is the position of the laser focal length relative to the sample surface, which determines the geometric dimensions of the hardened area.

The wear and corrosion resistance of AISI H13 tool steel laser hardened up to 800 HV was studied by Telsang et al. [17]. Thus, using a high-power diode laser with a maximum power of 2.5 kW, they were able to harden AISI H13 steel and characterize the influence of depth of hardness and surface melting. Because when the energy density is higher, the interaction of the laser beams with the surface and the hardness increases. The wear test results showed that the scratch resistance in the hardened areas was improved by 75 j/mm² compared to the base metal. A comparative study between two high-power diode and CO₂ lasers for hardening AISI 1045 steel was presented by Li et al. [18]. They evaluated the effect of each of the two lasers on the quality of surface hardening. They found that the high-power diode laser has a higher laser hardening quality than the CO₂ laser. Lo et al. [19] investigated the surface hardening of AISI 440C martensitic stainless steel using an Nd:YAG laser. In the laser surface hardening processes, the scanning speed varied from 25 to 85 mm/s. The hardness of the laser-hardened layer reached 600–800 HV at a depth of 100 μm under experiment conditions. The wear resistance of this steel improved significantly after laser hardening and increased by three times compared to other methods.

Pinahin et al. [20] used Nd:YAG solid-state to investigate laser surface hardening of various tool steels (T5K10, VK8, VK6, and T15K6). They assessed a depth of 0.2 mm from the distribution of high-energy laser beams and single pulses on these materials, which causes the formation of shock waves in the structure of the material. For the microstructural analysis of the material, wear tests, X-ray, and microhardness analysis were performed. It was found that higher wear resistance was obtained by performing laser surface hardening processes. Sadooghi et al. assessed the improvement of material properties and tribological and mechanical behavior of Mg-SiC nano/microcomposite [21]. Goia et al. [22] were among the researchers who used fiber laser for surface hardening of AISI D6 tool steel to increase the hardness of the base metal up to 800 HV. In this study, the hardening depth was about 1 mm below the sample surface. Martinez et al. [23] performed surface hardening with a high-power 1 kW laser on AISI 1045

steel. In this procedure, the laser scanning speed greatly influenced the hardness depth. The maximum microhardness in this study was 834 Hv.

One of the main challenges of laser surface hardening technology is the limitation of the hardening area whenever the laser scans the surface. The industrial development of high-power semiconductor lasers with high spot widths and overlapping hardened paths is two major solutions that have helped to address this problem [24, 25]. Research on high-power Nd:YAG laser transformation hardening has not been adequately studied, due to the traditional AISI4130 hardening process in the industry. Another goal of this research is to gain experience in this field by using modern and advanced equipment very close to the industrial process.

2 Experimental

In this study, an AISI 4130 steel sheet with dimensions of 10 × 10 × 2 mm³ was cut by laser and prepared to extract the basic parameters of LSH. Also, the quantum test Arc/Spark optical emission spectroscopy (OES) was performed on the sheet to determine the chemical composition accurately, as shown in Table 1. The laser used in this study is an Nd:YAG pulsed device (model A-600 with a maximum average power of 300 W). This laser can be produced pulses with a maximum power of 7000 W. The generated pulses can be executed in the frequency range from 1 to 40 Hz and the pulse width range of 5 to 45 ms. To match the execution conditions of the surface hardening tests with the real conditions for industrial samples, the head of the laser device is mounted on a 5-axis Kuka robot that controls the processing speed. Figure 1 shows a laser coupled to a robot and the equipment utilized to perform the laser hardening process. The final parameters range for laser hardening is given in Table 2.

It should be noted that for all four samples, the pulse width is 11 ms, and the square pulse shape was considered. Equation (1) shows the relationship between the average power (P_{AVG}) of the laser and the peak power, pulse width (D), and frequency (f). Equation (2) shows the heat input as a function of average power and welding speed (V) [26].

$$P_{AVG} = \text{Peak Power} \times D \times f \quad (1)$$

$$\text{Heat Input} = \frac{P_{AVG}}{V} \quad (2)$$

Finally, after this surface hardening, the specimens were cut into cross sections by wire-cut and mounted for metallography. For sanding, 120 to 5000 sandpapers were used manually. An alumina suspension solution with a particle size of 0.3 μm was used to polish the specimens. Polishing was performed with the polishing machine at a speed of 600 rpm.

Table 1 Average chemical composition of standard steel and studied steel (wt%)

Elements	C	Si	Mn	Cr	Ni	Mo	S + P	Fe
ASTM A29	0.28–0.33	0.15–0.35	0.4–0.6	0.8–1.1	Trace	0.15–0.25	0.07	Base
Elements	C	Si	Mn	Cr	Ni	Mo	S + P	Fe
Steel (4130)	0.242	0.186	0.49	0.836	0.005	0.174	0.018	Base

A 4% Nital solution (98% ethanol and 2% nitric acid) was used to etch the samples. An Olympus optical microscope (OM) and a scanning electron microscope (SEM), model MRA3 TESCAN equipped with EDS, were employed to study the microstructure of the samples. The microhardness instrument (MICROMET BUEHLER) with a load of 100 g was applied to measure the hardness of the samples. A wear test was performed with a pin on a disk with 5-mm-diameter pins made of 52,100 steel according to the ASTM-G99 standard [27]. The applied force, sliding speed, and total distance traveled in the wear test were 25 N, 0.5 mm/s, and 1000 m, respectively. Nevertheless, in the wear test, the circular diameter error caused by the wear test has been minimized, and the pin-on-disk wear test has been performed at a speed of 0.5 mm/s. Also, to increase the accuracy of the experimental results, each test has been repeated at least three times. Pins with a diameter of 5 mm were used to create wear tracks with a diameter of 5 mm on the samples. In this way, the error caused by the small width of the hardened area has been avoided.

3 Results and Discussion

3.1 Investigation of Base Metal Microstructure

Figure 2 shows the normalized microstructure of AISI 4130 steel at two different magnifications. The microstructure of AISI 4130 steel is mainly pearlitic–ferritic in such a way that perlite colonies were surrounded by ferrite grains. Due to the low carbon content in the structure, the percentage of ferrite grains is higher than that of the perlite grains. Also, the structure of the pearlite–ferrite is shown in Fig. 2b. In this band-shaped structure, pearlite strips are formed in the rolling direction. The main reason for the formation of pearlite strips is the dendritic separation of substitutional alloy elements during solidification [28, 29].

3.2 Microstructural and Metallurgical Study of Hardened Areas

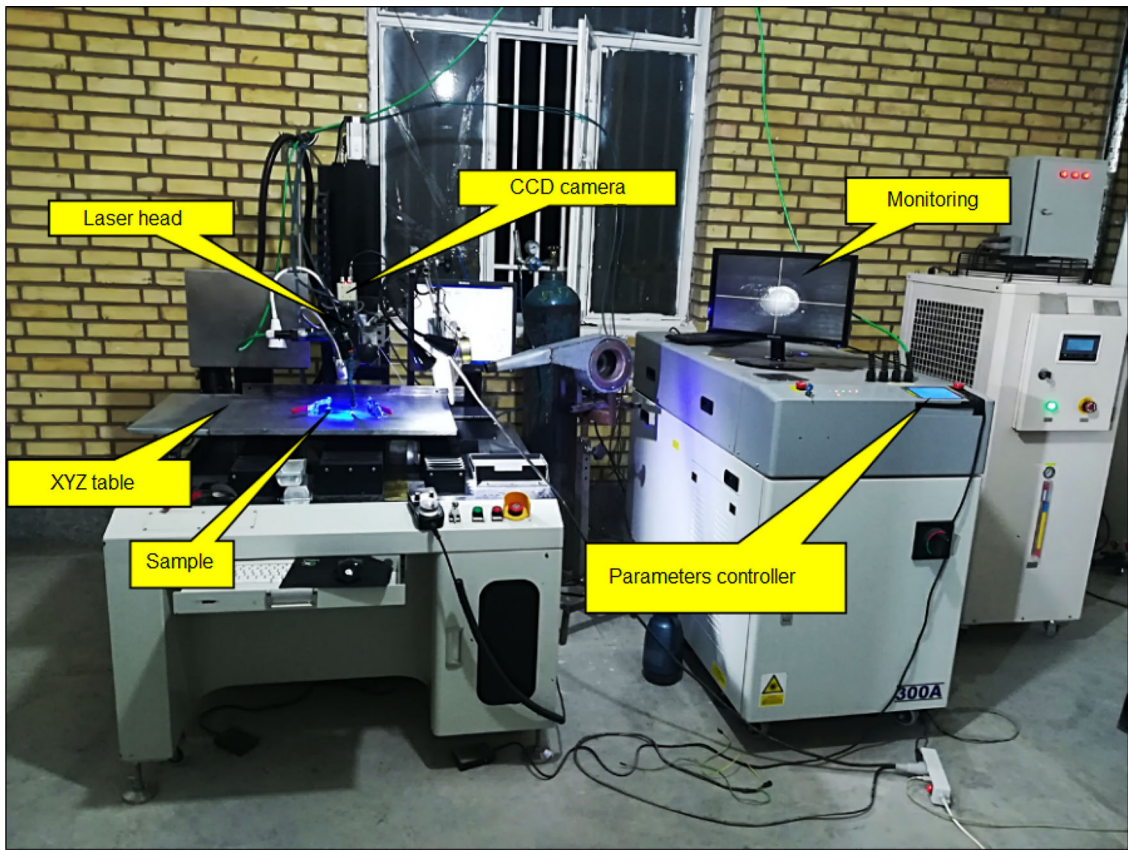
As can be seen in Fig. 3, the AISI4130 steel has two microstructural zones in the laser beam-affected area. Martensitic microstructures are observed beneath the surface

(Fig. 3c). From the curve of microhardness result, the maximum hardness value of the martensite area is 650 Vickers. As shown in Fig. 3a and d, the second transformed region was morphologically similar to the bainitic microstructures.

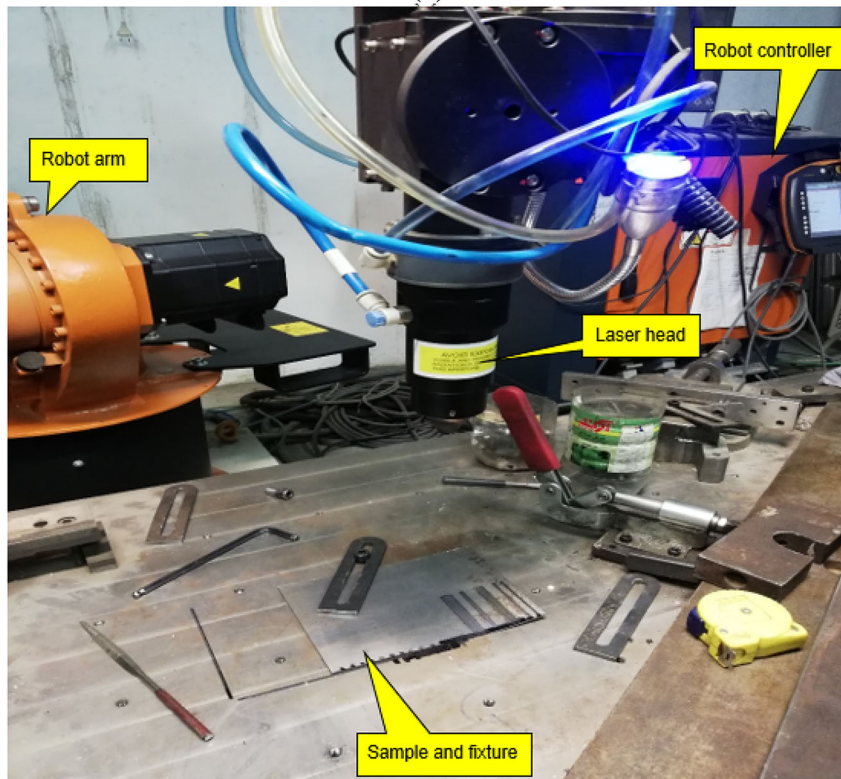
The process of laser transformation hardening creates beam-affected regions of separable and distinct microstructures in some ferrous alloys. Different microstructures in a laser-hardened cross section show that bainite structures are formed instead of martensitic structures in areas where the effective temperature–time decreases. In conventional heat treatment processes, the cooling rate is a major factor in microstructure formation. The cooling rate from the surface to depth has decreased based on simulated thermal cycles, but this reduction is not noticeable and predictable [30].

A critical factor that causes the difference between the microstructure at the surface and at the depth of the specimen can be discussed in terms of the effect of rapid thermal cycles on the hardenability of different regions. The hardenability of steel is affected by several factors. The grain size and chemical composition of the austenite phase are two main factors, especially in the LSH process [31]. As mentioned earlier, the effective temperature–time characteristic decreases from surface to depth during the surface transformation hardening process. Decreasing the effective temperature–time characteristic affects the formed austenite phase because more austenite grain growth occurs in areas with a high effective temperature–time, which increases hardenability. However, due to the lower effective temperature–time in the deeper austenitized areas, the austenite grain growth is lower than in the surface areas. Therefore, the hardenability in these areas is lower.

On the other hand, the effective temperature–time effect on the dissolution rate of alloy carbides and cementite leads to differences in the chemical composition of austenite in different regions. The chemical composition of AISI4130 steel contains carbide former elements such as Mg, Mo, and Cr. The presence of various alloying elements, except Co, in the chemical composition of the austenite phase increases the hardenability of the steel. The effect of alloy elements on the hardenability of the austenite phase is related to the presence of these elements in the solid solution of the austenite. Strong carbide former alloying elements are present in the chemical composition of AISI4130 steel, and the effective temperature–time characteristic cannot dissolve these carbides in all



(a)

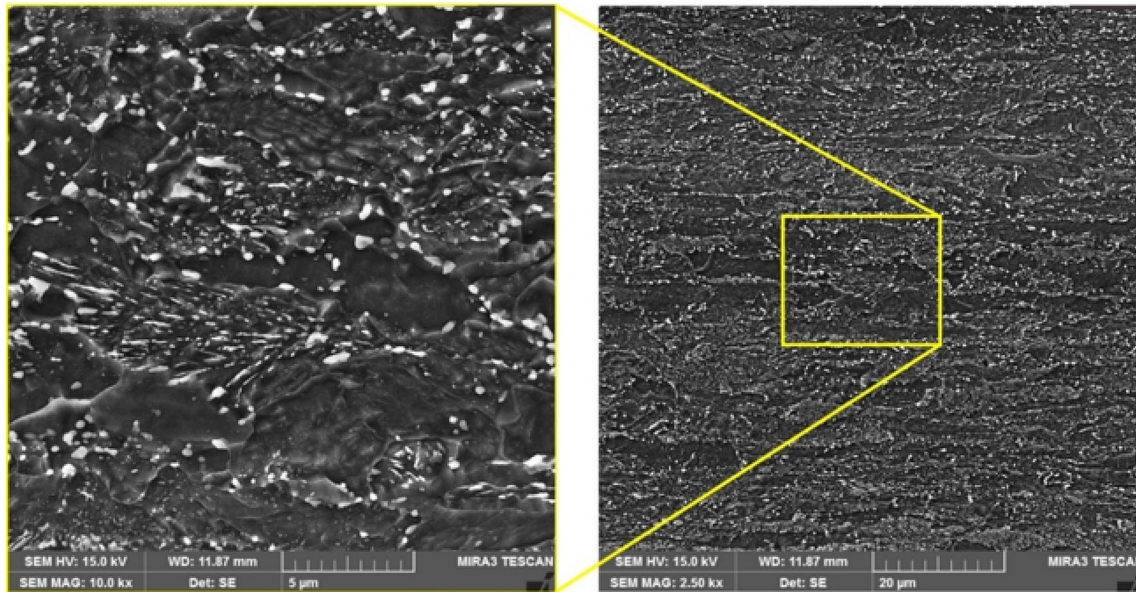


(b)

Fig. 1 **a** Equipment for the laser hardening process and **b** laser coupled with robots and

Table 2 Selected parameters for surface hardening with Nd:YAG laser

No	Pulse frequency (Hz)	Maximum power (kW)	Average power (W)	Out-of-focus distance (mm)	Heat input (j/mm)	Scanning speed (mm/s)
LH-1	10	2.3	235	10	47	8
LH-2	7	3.5	264	10	52.8	5
LH-3	10	2.3	235	20	47	8
LH-4	7	3.5	264	20	52.8	5

**Fig. 2** SEM image of AISI 4130 steel microstructure including pearlite and cementite phases

areas of the heat-affected zone (HAZ). Therefore, the presence of carbide former alloying elements not only leads to an increase in hardenability in these areas, but the undissolved carbides can act as pearlite phase nucleation sites, which can reduce the hardenability of the steel. Thus, the probability of exceeding the cooling rate in HAZs increases and causes bainite microstructures to be observed even during rapid surface heat treatment processes.

Figure 4 shows the microhardness curves of the cross-sections of the different areas in the sample LH-2 of AISI4130 steel. This curve shows the maximum hardness in the surface areas up to a depth of 50 microns. According to the microstructural images, the martensite microstructure is dominant in this region. Then, at a depth of 50 to 100 μm , a two-phase martensite–bainite microstructure gradually forms. The microstructure is bainitic at a depth of 100 to 200 μm , and the hardness gradually decreases with depth in this region. Hardness drop could be attributed to the reduction of the cooling rate in the thermal cycles and the reduction of the effective temperature–time of austenitization.

3.3 Effect of Beam Scan Velocity

Beam velocity is a very effective variable in the surface hardening process. This factor can control the interaction time of the laser beam with the surface, the heating and cooling rates, the input energy, and the efficiency of beam absorption. Thus, beam velocity affects properties such as penetration depth, surface roughness, the microstructure of HAZ, and surface hardness [32]. For specimens with longer focal lengths or higher beam velocities, the hardened region exhibits a uniform microstructure similar to that of a bainitic structure. A closer examination of the microhardness of the LH4 sample revealed a significant difference between the hardness results at the surface to the depth. As can be seen in Fig. 5, in the uniform zone of the bainite phase at the same magnification, the differences in microstructure could be seen from the surface to the depth of the hardened area. The cross-sectional image of the sample LH-4 is shown in Fig. 5. To observe the microstructure differences, micrographs were taken at 50-micron intervals in each section at the same magnification. Comparing the sample LH-2 with the sample LH-4, it could be seen that by decreasing the speed movement of the laser

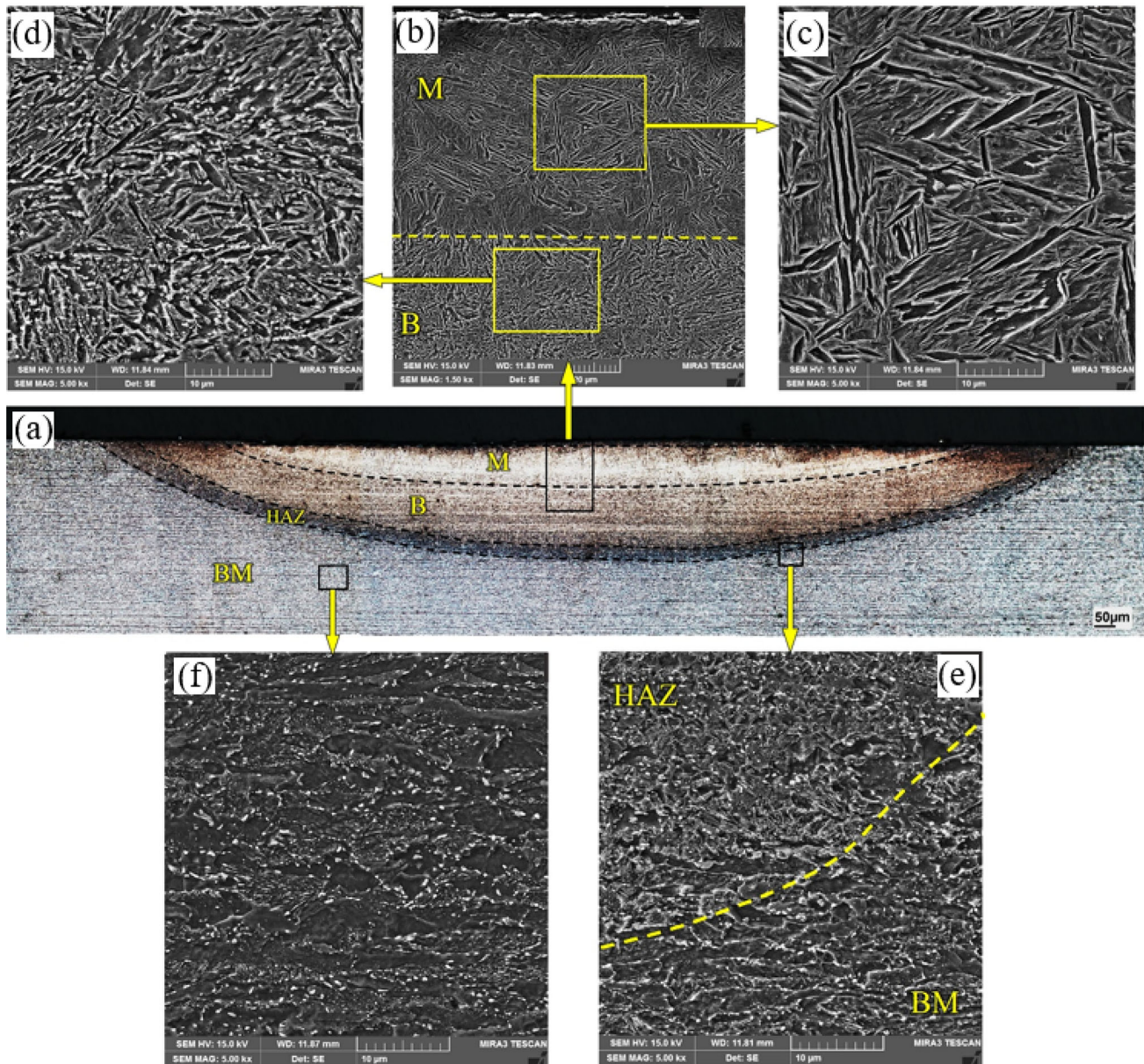


Fig. 3 **a** Optical microscope image of the hardened cross-section of the LH-2 sample of AISI4130 steel with Nd:YAG laser, including areas M (martensite), B (bainite), HAZ (heat affected zone), and BM (Base metal) with a beam velocity of 5 mm/s and distance outside the focus

10 mm, **b** SEM image of martensite and bainite areas, **c** SEM image of martensite structure at higher magnification, **d** SEM image of the bainite phase at higher magnification, **e** SEM image of the HAZ and its boundary with the base metal, **f** SEM image of base metal

beam on the workpiece, the hardness of the beam-affected surface area has been increased.

Up to 50 microns from the surface, the few islets of martensite are distributed in the main structure of the bainite structure. At higher magnifications, very fine martensite blades (plates) could be seen with relatively parallel layers and unresolved carbides trapped between the blades. At a distance of 100–50 microns from the surface, the distribution of cementite particles exhibits an angle to the growth direction of ferrite grains, known as lower bainite. The ferrite matrix

has a suitable and scattered distribution of cementite particles at a distance of 100–150 microns from the surface, which is called as upper bainite. In these areas, the cementite particles are in the direction of ferrite grain growth. Then, the formation of the transition zone between upper bainite and base metal is observed, which contains relatively large carbides in the structure.



Fig. 4 Microhardness curve of the cross-section of different areas consisting of surface to a depth of LH-2 sample of AISI4130 steel including martensite, bainite, HAZ, and base metal, respectively

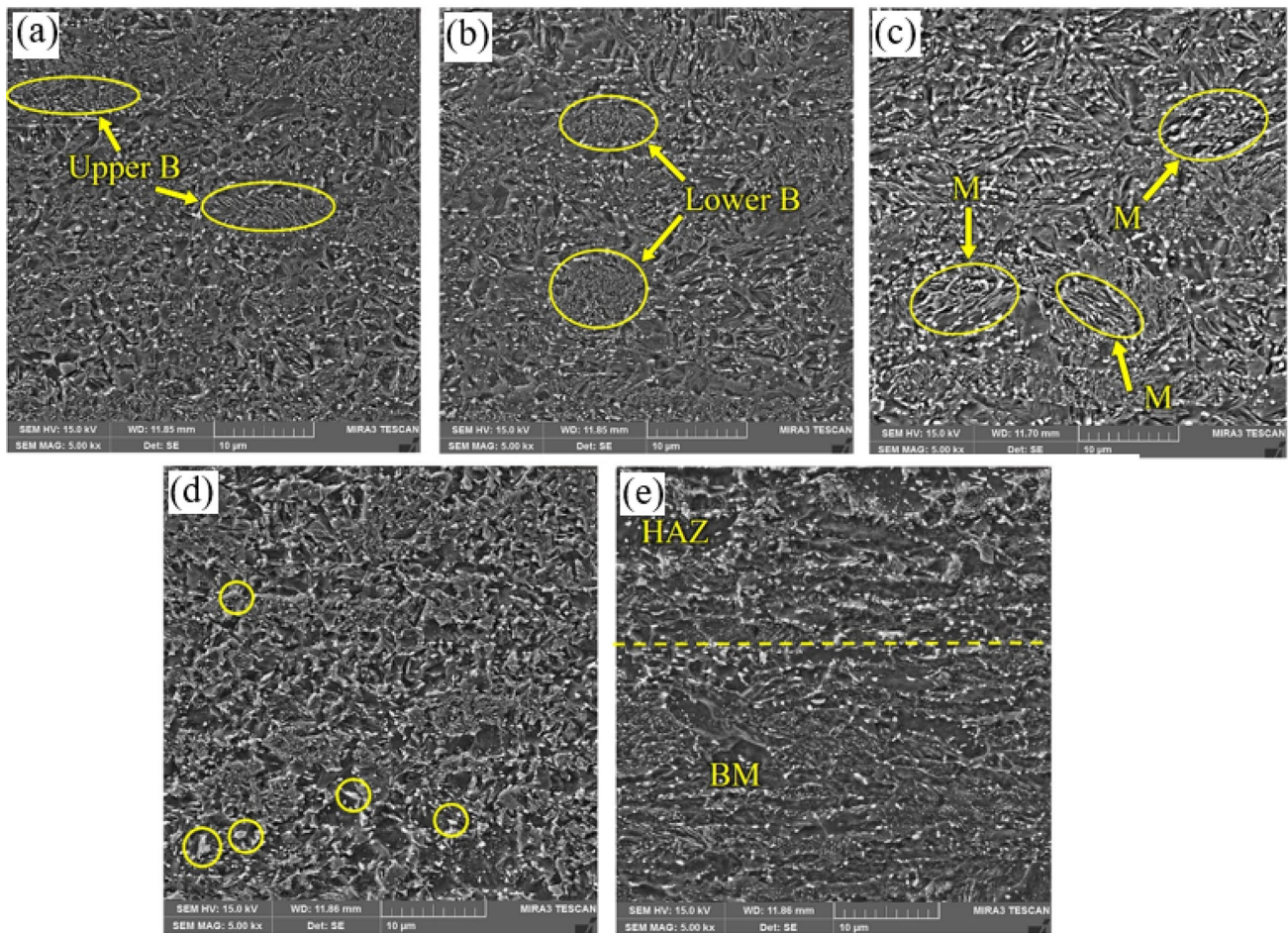
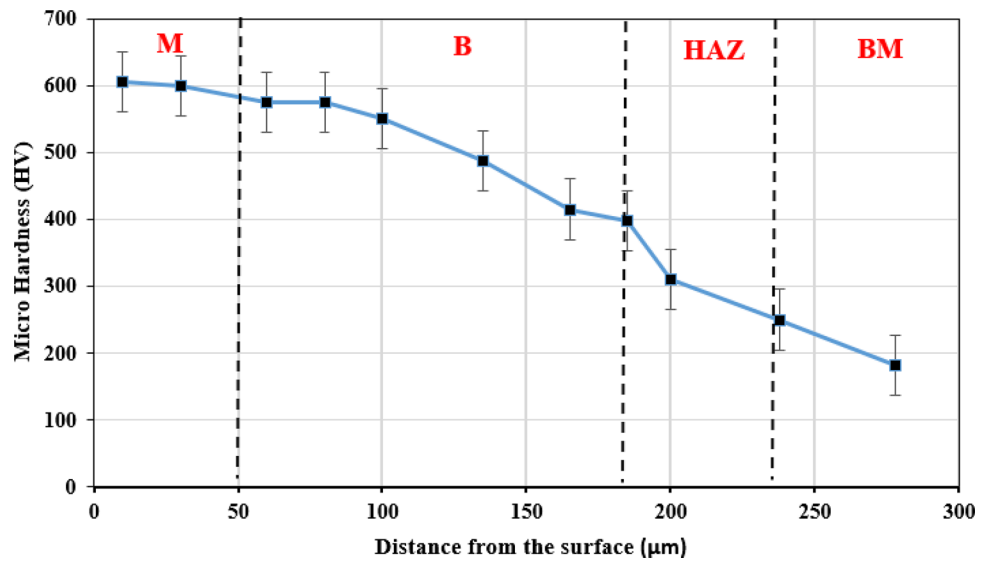


Fig. 5 Microstructure of LH-4 sample cross section from surface to the depth at 50-μm intervals, **a** presence of layered martensite at (0 –

50 μm), **b** fine bainite structure at (50–100 μm), **c** coarse bainite structure at (150–100 μm), **d** the distribution of carbides at (200–150), and **e** the interface of the hardened layer with the base metal at (200–250 μm)

3.4 Effect of Out-of-Focus Distance

One of the other effective variables in the LSH process includes out-of-focus distance. The focal length of the laser was considered to be 250 mm. Reducing the out-of-focus distance increases the power density and depth of the hardened area as well as the penetration depth. The beam power density and power distribution change as the focal length increases. Indeed, by decreasing the out-of-focus distance, the power density, and the hardened depth increase. Finally, it can be said that the maximum hardened depth was obtained in the samples that had the lowest beam scanning speed, the lowest focal distance, and the highest power intensity. Furthermore, laser power, power density, and hardening depth increase whenever travel speed decreases. Heat input increases when the laser power increases and the scanning speed decreases. Increases in the heat input lead to increases in the hardness. Moreover, by reducing the radius of the spot diameter, a maximum hardened depth could be acquired. According to the results of this research, it was observed that a sudden decrease in penetration depth occurred with an increase in out-of-focus distance from 10 to 20 mm. Also, the highest hardening depth was obtained in the sample with the shortest focal length and, consequently, the lowest beam velocity and the highest power intensity.

From the hardening results with different beam velocities, it has been observed that the depth of the hardened area has decreased with increasing the laser beam velocity. As the scan speed of the laser beam decreases, the interaction time of the laser beam with the material surface increases. This resulted in the laser beam having more time to excite the surface atoms, which increased the surface temperature [33]. The interaction time can be increased by increasing the width of the laser spot and reducing the scanning speed of the laser beam, which increases the energy content. Increasing the surface irradiation time allows for deeper heat penetration and provides kinetic and thermodynamic transformation conditions for deeper points from the surface. The energy content can be increased both by increasing the scan speed of the beam and by increasing the power of the beam. Studies show these variables should be within a reasonable range [34, 35]. In this way, if the density power of the beam is more than a specific value, it will cause the surface to melt or reduce the depth of the hardened area. On the other hand, the interaction time of the beam with the surface must be within a certain range because an excessive increase in this characteristic can also increase the risk of surface melting [36, 37].

As mentioned earlier, one of the major challenges of laser surface hardening technology is the limitation on the width of the hardening area whenever the laser beam scans the surface. To overcome this problem, hardened paths are placed next to each other. Due to the thermal effects, the adjacent path leads to the temper of the previously hardened area,

which decreases the hardness properties in the previously adjacent hardened area. Therefore, the hardness properties in the laser-hardened surface area are non-uniform [24]. The presence of supersaturated carbon in the BCT crystal, dislocations, and twins in the crystal structure of the martensitic plates and the surface energy resulting from the high interface between the martensitic plates leads to the instability of the martensite microstructure. Therefore, thermal cycles in the surface hardening process affect the previously hardened areas and lead to a decrease in mechanical properties. Some studies have mentioned this problem for induction hardening methods using flat inductor rings [38–40]. The heat treatment cycle of the tempering process at temperatures below A_{c1} is defined. Tempering generally occurs in three stages: the formation of transition carbides such as ϵ and η carbides (100–250 °C), the transformation of residual austenite to ferrite and cementite (200–300 °C), and the replacement of transition carbides and low carbon martensite by ferrite and cementite (the beginning of the third stage of tempering is in the temperature range of 250–350 °C) [32, 41].

3.5 Overlap Effect

Figure 6 shows the surface of two laser surface hardened samples, LH-2 and LH-4, with a 20% overlap. The maximum hardened depth was observed for AISI4130 steel during transformation surface hardening with a speed of 5 mm/s and out-of-distance 10 mm. For this reason, these variables have been used to investigate the overlap effect. Figure 7 shows the cross section of the area affected by the laser beam in three laser paths with 20% lateral overlap. Also, as can be seen in Fig. 7(a), a cross section of three paths, including No.1, No.2, and No.3, with a 20% overlap was shown. In this regard, for a better understanding, the interface of two passes, No.1 and No.2, is also displayed in higher magnification. This is designated with A in Fig. 7(b) and (c). In the vicinity of path No.1, due to the re-passing of path No.2, in the interface of the two paths, temper treatment has occurred. Finally, the hardness of path No.2 due to the tempered area is lower than that of the surrounding areas in the vicinity of the paths interface. The observations indicate that the thermal effects of adjacent paths cause reheating around the previously hardened area. Therefore, the microstructure of the area changes and slightly decreases the hardness properties in those areas that cause non-uniform surface properties, which is not very desirable. In addition, microhardness changes were investigated by increasing the overlap up to 50%, and the results of this process are presented in the next section.

3.6 Microhardness Results

Figure 8 shows the microhardness curve of the LH sample at a depth of 50 microns from the surface. Accordingly, the

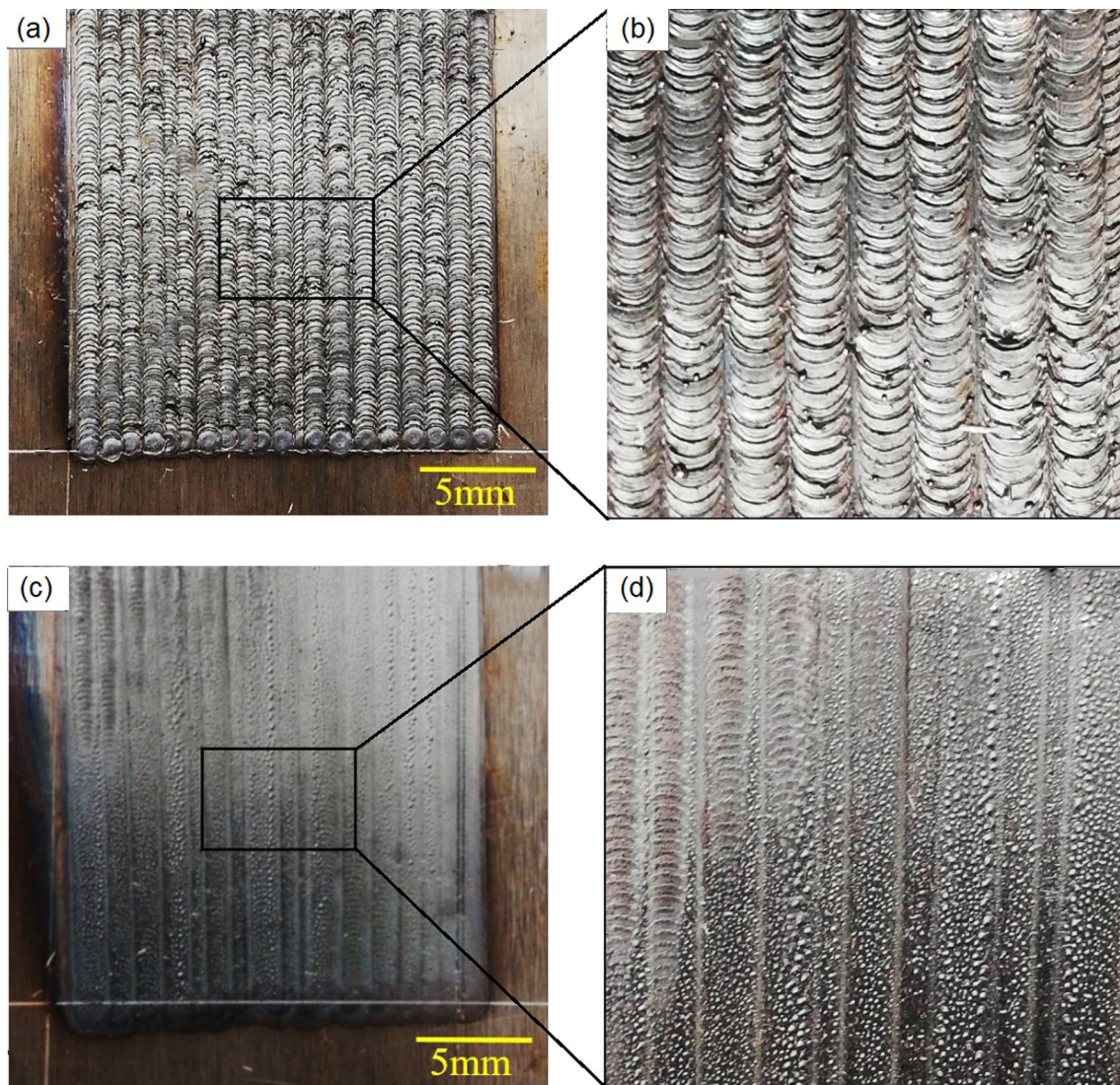


Fig. 6 **a** Surface image of LH-2 sample hardened with Nd:YAG laser, **b** higher magnification of 20% overlap of the passes (LH-2 sample), **c** surface image of LH-4 sample, and **d** higher magnification of 20% overlap of the passes (LH-4 sample)

hardness changes of the hardened path No. 1 should be similar to the hardness curve of the area affected by the single path beam. On the other hand, a slight decrease in hardness is observed in the adjacent areas, path NO. 2. The lower hardness of path No.2 is related to the tempered area that occurred with the re-passing of the laser in the vicinity of path No.1. In this case, the martensitic structure and instability formed in the first step in pass No.2 have changed with the passing of the laser beam. The ferrite and cementite phases have replaced transition carbides in the final tempering step. However, due to the high cooling rate in this process and the lack of sufficient temperature due to the short interaction time, the transition carbides did not have enough time for structural transformation.

Hardness behavior was observed at a depth of 100 μm from the surface of the hardened area, which is in good

agreement with the results of the previous studies [24, 25]. The effect of overlap on induction hardening of AISI4140 steels was reported by Cordovilla et al.[25]. They reported an overlap effect on chromium-molybdenum steels based on induction hardening, similar to the laser hardening method. Indeed, the reduction in hardness values is related to the thermal cycles imposed from the adjacent hardened area, which during a rapid thermal cycle causes metallurgical changes. The rate and temperature of the thermal cycles in the tempered regions are much higher than that in the tempering thermal cycles in the normal state.

Increasing the percentage of overlap to 50% is expected to decrease the difference in the hardness of the last scanned path of the beam-affected areas compared to the sample with 20% overlap. At the same time, the same procedure is expected for the hardness results. The lower hardness drop

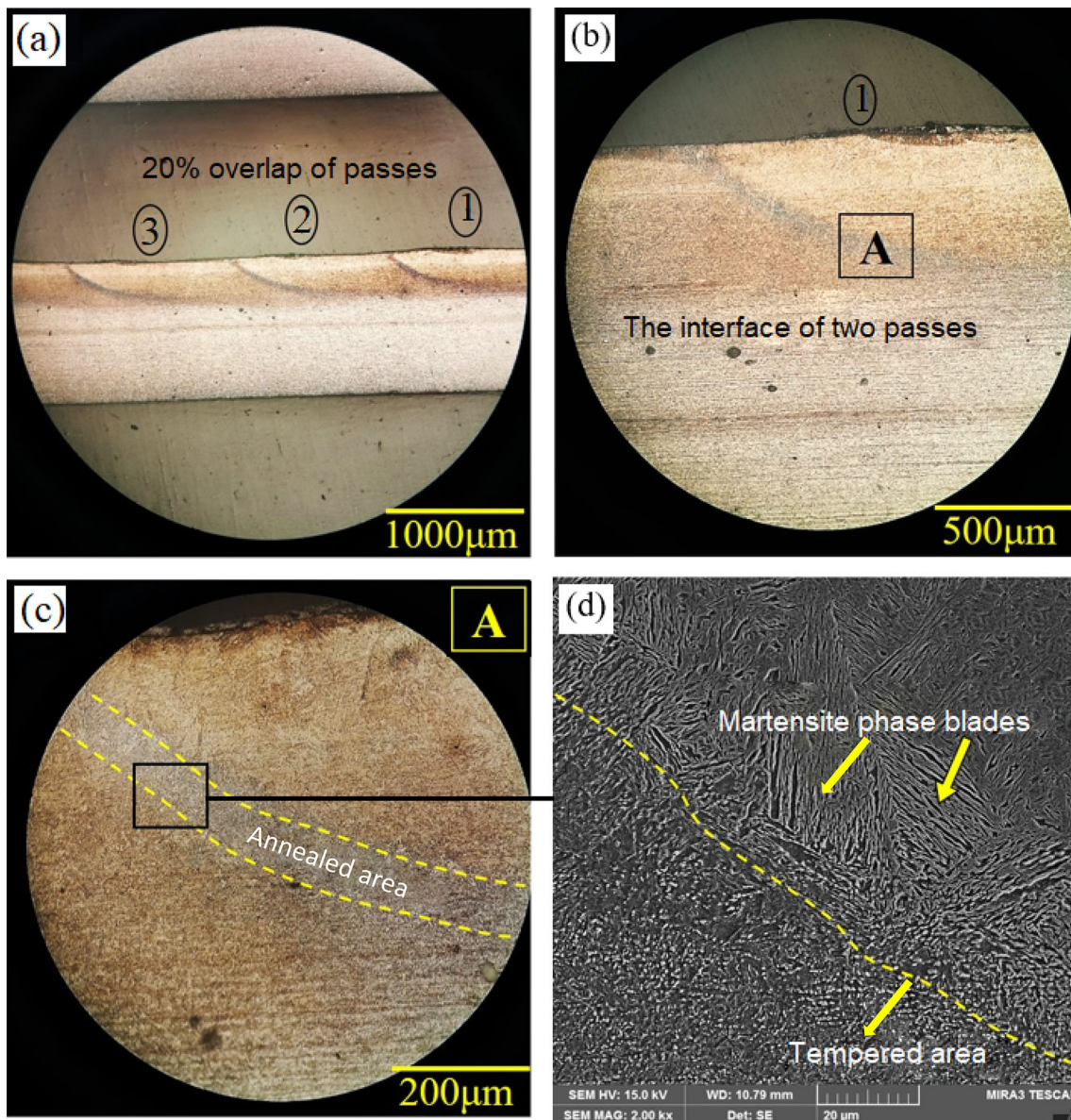


Fig. 7 **a** Optical microscopic image of the cross section of the three paths of the hardened sample (LH-4) with 20% overlap, **b** higher magnification of the interface of passes No.1 and No.2, **c** higher magnification of area A in part b, and **d** SEM image of the tempered area boundary

can be attributed to the difference in the microstructures formed in the adjacent areas compared to the more central regions during the laser hardening process. With 20% overlap, adjacent area thermal cycles are experienced in regions of the heat-affected zone that experience less heat input. Therefore, the undissolved carbides in these areas can be easily recognized in these regions. However, due to the thermal cycle with a higher temperature–time factor, the central regions exhibit a more uniform microstructure, resulting in less hardness loss.

3.7 Wear Results

As mentioned earlier, by reducing the scanning speed of the laser beam, the interaction time of the laser beam with the surface of the material is prolonged. As a result, the heat generated by the radiation of the laser beam has more opportunity to penetrate into the depth. Therefore, kinetic and thermodynamic transformation conditions are provided for the deeper points. For this reason, hardened samples with lower scanning speeds (LH -2 and LH -4) were selected for the wear tests, and the effect of out-of-focus distance was investigated.

Figure 9 shows the average coefficient of friction for specimens that have been subjected to the wear test. The friction

Fig. 8 The microhardness curve at a depth of 50 μm from the sample surface with 20% overlap

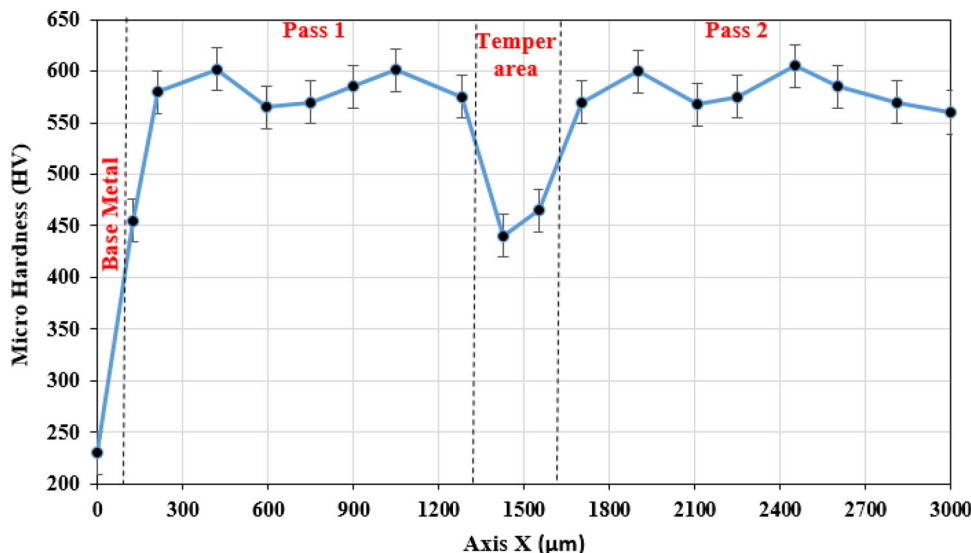
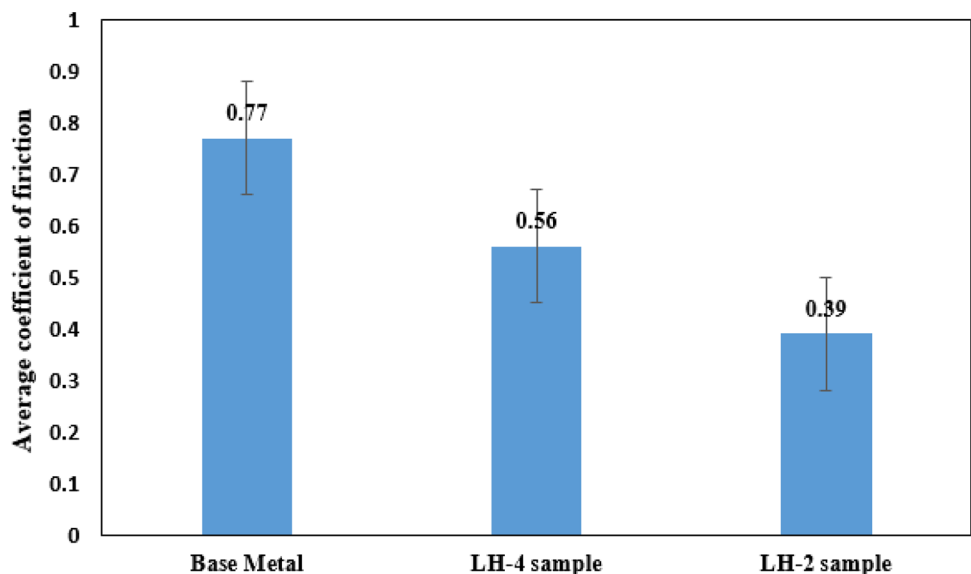


Fig. 9 Graph the average friction coefficient in hardened specimens at a different distance outside the focus by laser and the base metal specimen



coefficient values for base metal, LH-4, and LH-2 samples were obtained at 0.77, 0.56, and 0.39, respectively. Furthermore, three repeated friction experiments were performed on the material, and the average value and standard deviation of the friction coefficient at different samples were obtained, as shown in Fig. 9. The friction coefficient is the ratio between the measured friction force during sliding and the applied load. The results show that the coefficient of friction of all laser-hardened samples is lower than that of the base metal sample, which can be attributed to the high surface hardness of laser-hardened samples compared to the base metal.

On the other hand, by reducing the scanning speed the interaction time of the laser and material will be enhanced. Increases in the heat input lead to increases the hardness. Thus heat input increases when the laser power increases and the scanning speed decreases. It is also observed that the

coefficient of friction of the LH-2 sample is lower than that of the LH-4 sample. The maximum hardness is approximately 650 HV in laser surface hardened with 10 mm out-of-distance (LH-2). As indicated in Fig. 4, as the distance from the surface increases, the hardness decreases, and consequently the coefficient of friction increases. The coefficient of friction was reduced by 27.3% and 50% in LH-4 and LH-2 samples with respect to the base metal. Also, the friction coefficient of sample LH-2 has decreased by 30% compared to LH-4 due to the reduction of the focal distance.

During the wear tests, the coefficient of friction was continuously recorded and plotted against sliding distance (m). A total sliding distance of 1000 m was kept in all the samples. Figure 10 shows the friction coefficient changes as a function of slip distance in the base metal, LH-4, and LH-2 samples. All three curves consist of two distinct stages, which are (1)

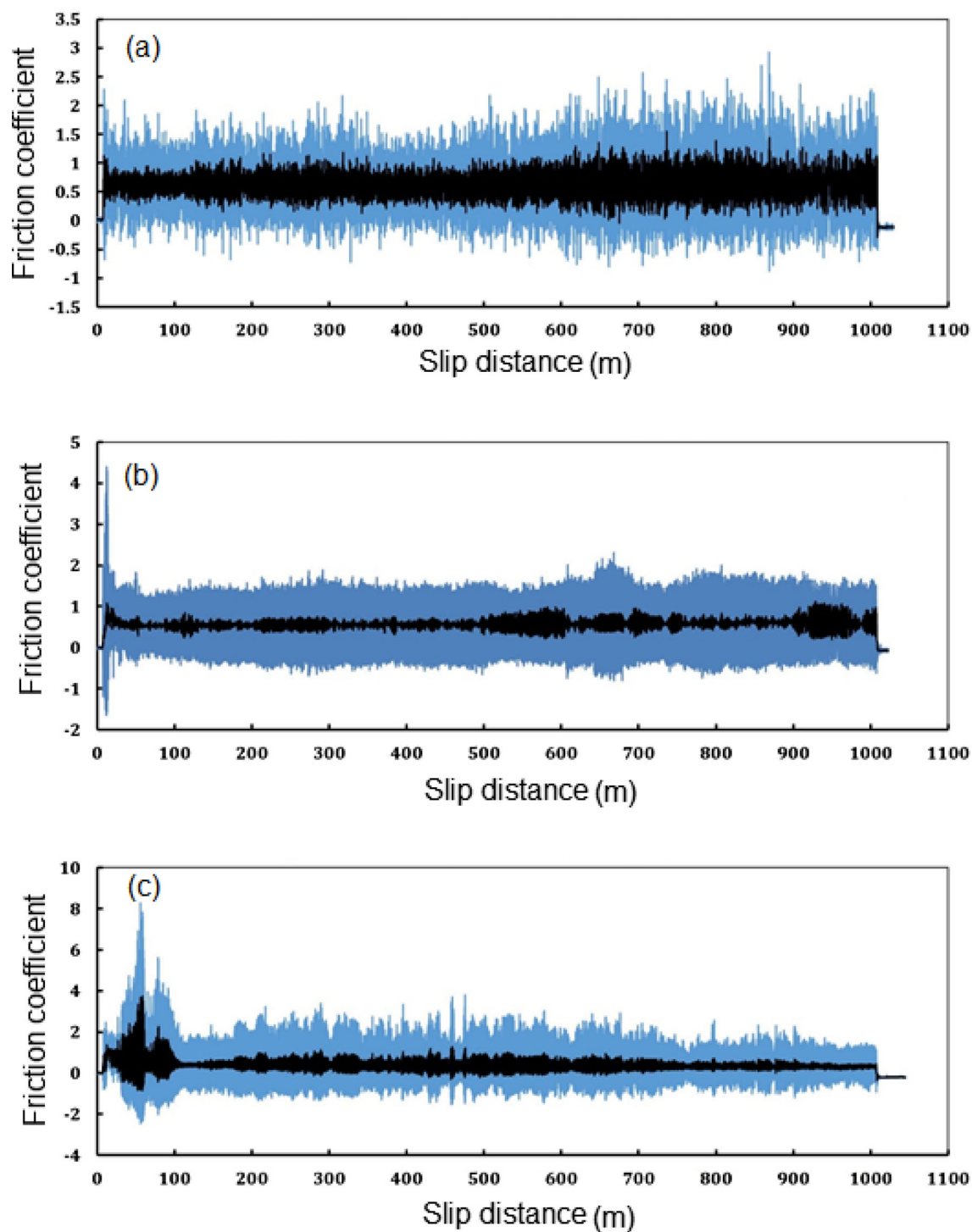


Fig. 10 Diagram of friction coefficient changes in terms of slip distance in (a) base metal, (b) hardened sample in LH-2, and (c) hardened sample in LH-4 sample

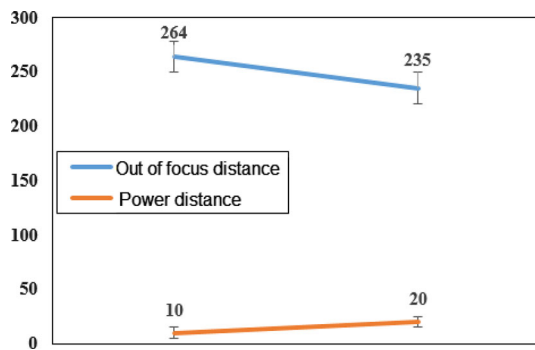


Fig. 11 Distance outside the focus and power density diagram in LH-2 and LH-4 samples

running-in wear or transition step and (2) steady-state wear. Initially, the friction coefficient increases with distance to a maximum and then decreases to achieve a steady state. However, the distance to the steady state may differ in the three specimens. As shown in Fig. 10 (a), the friction coefficient increases after a short distance when the base metal is subjected to a wear test and tends to reach a steady state. This observation is due to the gradual flattening of the asperities with sliding distance and increasing the contact area. While in the LH-2 sample, the coefficient of friction is initially low, and after a distance of approximately 500 m, the coefficient of friction increases. This was attributed to the brittle particles being removed from the sample's surface and placed in the wear path. However, for the LH-4 sample (with a distance outside the focus of 20 mm), the reduction in the coefficient of friction is not noticeable, and many fluctuations are observed at the beginning of the wear path. Because in samples with a greater distance outside the focus or where the scan speed of the beam is very high, a uniform structure was created in the HAZ. However, the microstructure is bainite, which has a lower hardness than a hard martensite structure. This can lead to an increase in the coefficient of friction compared to the hardened sample with a smaller distance outside the focus.

According to the diagram in Fig. 11, it can be seen that the power density decreases with increasing the distance outside the focus, resulting in a decrease in penetration and hardening depth. Therefore, it can be mentioned that the increase in friction coefficient from the LH-2 to the LH-4 sample is due to the decrease in hardness depth. The surface of the samples was examined by scanning electron microscopy (SEM) to determine the wear mechanism. Electron microscope images of the wear surfaces of the base metal, LH-2, and LH-4 samples are shown in Figures. 12 and 13. According to Fig. 12, when the specimens are subjected to a wear test, due to the surface roughness, the interaction between the surfaces and the pin increases, the connection between the two surfaces is

detached, and adhesive wear occurs. Since there is no protective layer on the surface, the surface of the specimen and the pin of the device are in direct contact, and rough surfaces and wear debris are created, which can be considered as adhesive wear.

In other words, the surfaces on the microscopic scale are completely rough. When these surfaces are placed opposite each other, and an external force compresses them, due to the very low ratio of in contact surfaces compared to the total surface, very high stress is applied to the rough surfaces. Owing to high-stress, local welds are created by mechanical or metallurgical connections. The base metal sample has poor wear resistance and adhesive wear, as shown in Fig. 12, because the hardness is low due to the lack of surface hardening.

In addition, the effects of scratches and dullness on the surface can be easily seen, which is a reason for abrasive wear mechanism. The mechanism of abrasive wear rarely occurs unless a very hard surface is placed in front of a surface with very low abrasion resistance [42, 43]. Due to the low hardness and lack of any hardening process, a significant reduction in mass is observed after the wear testing of the base metal. It was found from SEM micrographs that due to the lower wear rate, the wear resistance of laser-hardened specimens increases compared to the base metal specimen.

The parallel grooves created on the surface, as shown in Fig. 13, indicate abrasive wear. Also, according to the SEM micrographs of wear surfaces, the surface roughness on the wear surfaces of the hardened LH-4 sample was higher than that of the LH-2 sample, which is related to the lower wear resistance and brittleness of the specimen. Thus, it could be pointed to a direct relationship between hardness and wear resistance. Although adhesive wear occurred for the samples, which is not a suitable phenomenon for the tribological behavior of the material. However, as the hardness of the samples increases, the dominant wear mechanism tends to shift from adhesive wear to abrasive wear. The wear surfaces indicated oxidation along with signs of adhesive wear. Figure 13 (c) and (d) shows a higher magnification of the adhesive wear that occurred than in Fig. 13 (a) for LH-2. Due to the higher hardness of LH-2 compared to the base metal, fewer detachment particles have been observed. Consequently, the wear resistance of LH-2 is higher than other samples and causes less weight loss. Figure 13 (e) and (f) shows a higher magnification of the adhesive wear that has occurred than in Fig. 13 (b) for LH-4. As can be seen, the adhesive wear mechanism is dominant in LH-4 sample. This is because the hardness of LH-4 is less than LH-2, and it has less wear resistance. In general, the adhesive wear for the LH-2 sample is lower than for LH-4 and base metal samples which is consistent with the hardness measurement and weight loss results. Based on the observed results, it can be said that the dominant wear mechanism for the base metal samples, LH-4 and LH-2, the hardness of the samples increase, respectively. Moreover, the

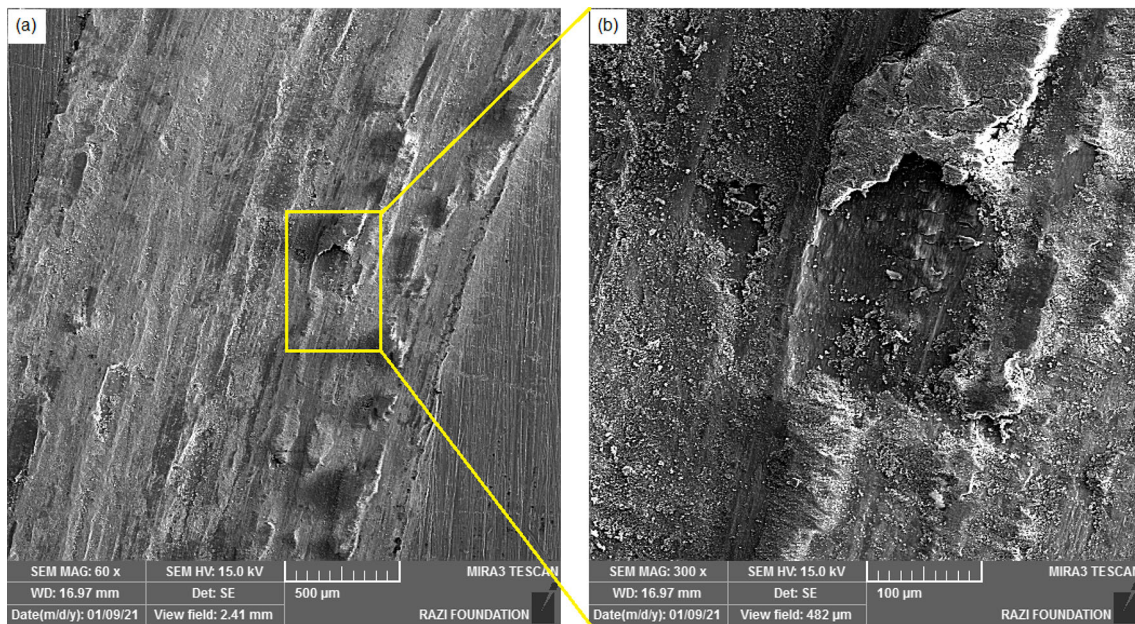


Fig. 12 SEM image of the wear surface of the base metal sample

adhesive wear mechanism tends to be the abrasive mechanism, and a combination of both mechanisms was detected in the hardened specimens.

Figure 14 shows the weight loss of the specimens during the wear test. According to the results, the weight loss of the LH-4 and LH-2 samples were 0.0085 g and 0.0062 g, respectively, but no significant difference was found in the width of the wear zone. As can be seen, the weight loss in the hardened sample LH-4 was higher than the LH-2. Although due to the higher wear rate and weight loss, a greater width of the wear zone should be obtained. However, no significant difference in the width of the wear zone was observed. This can be considered as the result of the lack of significant difference in weight loss, and for more detailed investigations, it is necessary to use accurate measurement software. Rough surfaces and metallic wear particles were created during the wear test. Due to this observation, the mechanism of wear that occurred in this stage can be considered excessive or severe adhesive wear so that the abrasive pin causes the galling material on the surface. Galling is a form of wear caused by adhesion between sliding surfaces. In the following stages, the results illustrate the tendency of abrasive products to adhere to the material surface, and the inclination to adhesive wear mechanism increases. In other words, on a microscopic scale, the surfaces are entirely rough, and micron roughness covers the entire surface.

When the wear test was performed on laser-hardened specimens in overlapping passes, it was observed that the wear resistance of the hardened LH-4 in single-pass mode was higher than the LH-2 sample. It can also be found that the

wear resistance of LH-4 was lower than that of the LH-2 sample, which based on electron microscope images, as shown in Fig. 15, obtained from their wear surfaces, the surface roughness of LH-4 is higher than the LH-2 sample.

4 Conclusion

This research investigated the hardness of laser transformations on AISI4130 steel with a thickness of 2 mm using high-power Nd:YAG pulsed laser technology. The surface of AISI4130 steel can be hardened to a depth of 0.4 mm and a width of 2 mm using an Nd:YAG laser with a maximum power of 3.5 kW, a distance outside the focus of 10 mm, and a speed of 5 mm/s. During this process, martensite and bainite microstructures are formed from surface to depth with a maximum hardness of 650 and 530 HV, respectively. The temperature–time characteristics in the hardened regions affect the rate of carbide dissolution and properties of the formed austenite. Comparing the specimens LH-3 and LH-4, it was found that the time of interaction of the beam with the surface increases with the speed of the laser beam on the workpiece. Finally, the surface hardness of the heat-affected zone increases so that the maximum hardness in this study is 834 Vickers.

In contrast, the hardened region exhibits a uniform microstructure that resembles the bainite structure for specimens with longer focal lengths and higher scanning speeds. It is expected that increasing the percentage of overlap to 50% will reduce the difference in hardness of the last scanned path of the beam-affected areas compared to the sample with

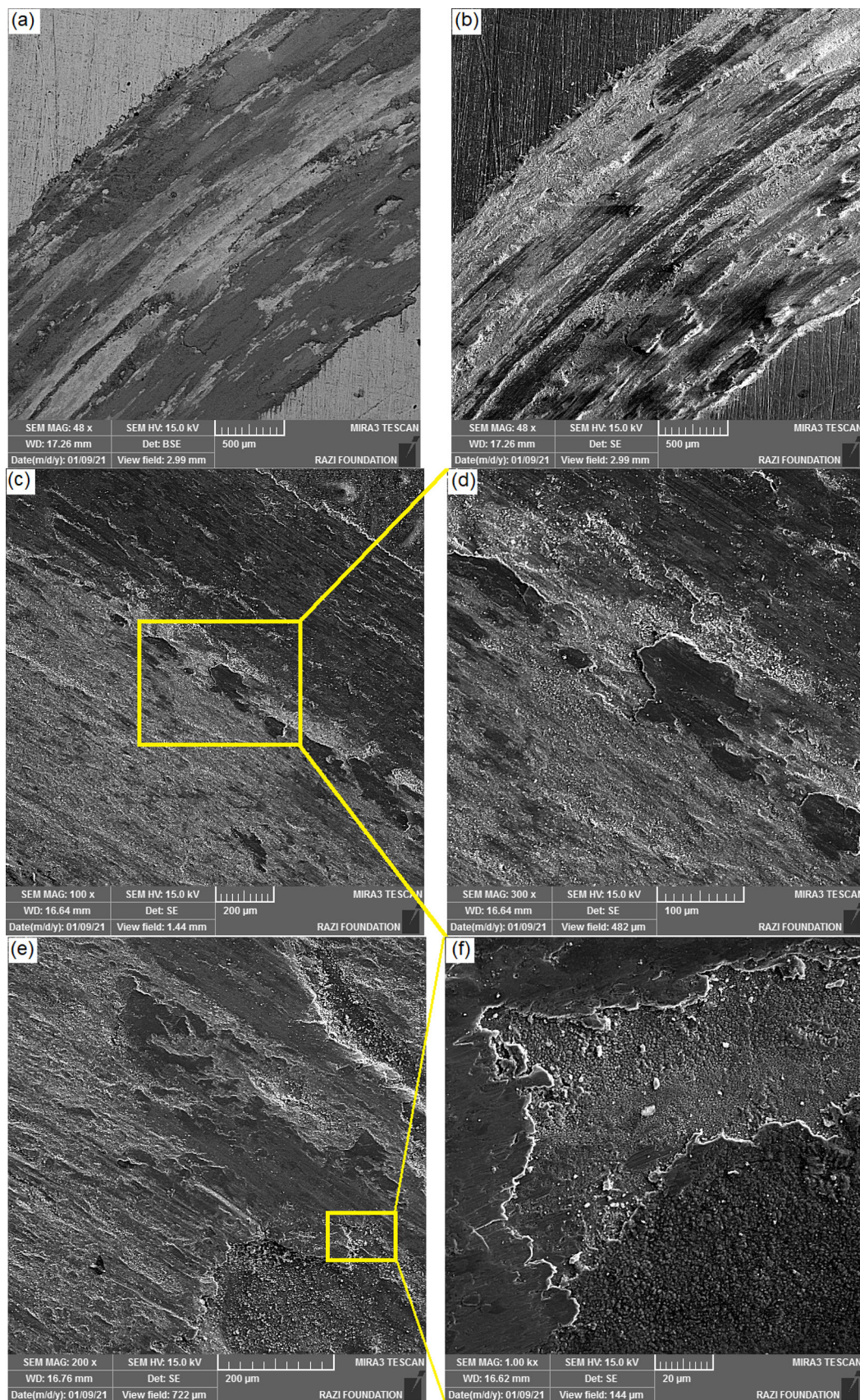


Fig. 13 SEM images of wear surfaces of hardened specimens at distances outside the focus **a** 10 mm and **b** 20 mm, **c**, **d** SEM image of the LH-2 at higher magnification, **(e-f)** SEM image of LH-4 at higher magnification

Fig. 14 Diagram of the difference between final and initial weight loss of specimens

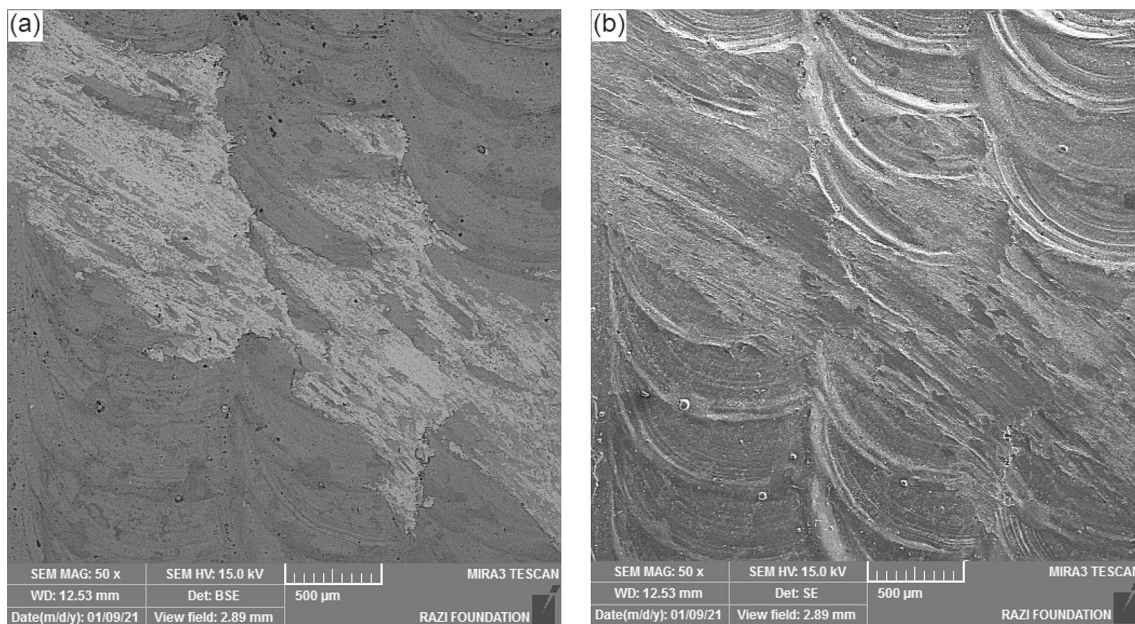
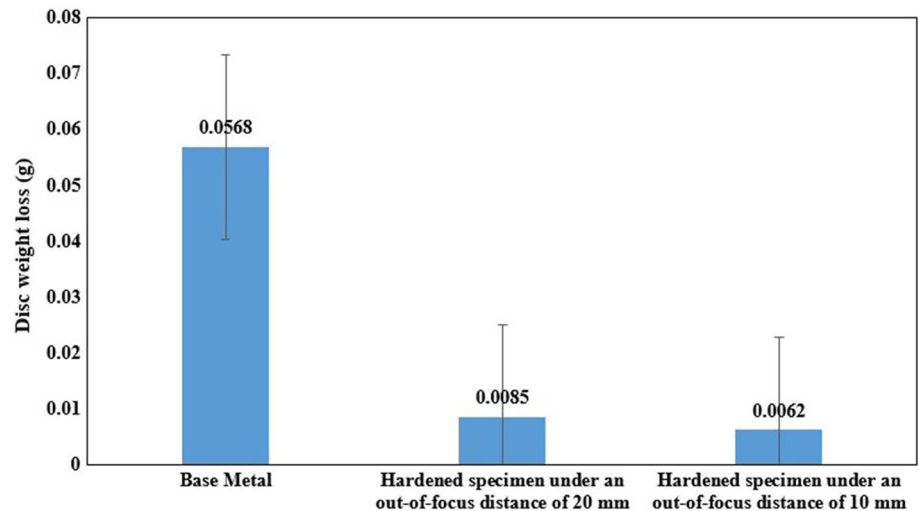


Fig. 15 SEM images of wear surfaces of hardened specimens under overlapping passes and distance outside the focus **a** 20 mm and **b** 10 mm

20% overlap. The laser-hardened samples were subjected to a pin-on-disk wear test due to the higher depth of hardness, and it was revealed that the friction coefficient of the base metal (0.77) decreased to 0.39 and 0.56 in the LH-2 and LH-4 samples, respectively. It can be mentioned that the increase in friction coefficient from the LH-2 to the LH-4 sample is due to the decrease in hardness depth. The wear resistance of the surface roughness on the wear surfaces of the hardened LH-4 sample was higher than that of the LH-2 sample, which is related to the lower wear resistance and brittleness of the specimen. A combination of abrasive and adhesive wear was shown in the wear surface of the laser-hardened samples. Due to the lower wear rate, the wear resistance of laser-hardened specimens increases compared to the base metal specimen.

A combination of abrasive and adhesive wear showed in the wear surface of the laser-hardened samples.

Acknowledgements None.

Authors' Contributions AFK conceived and designed the analysis and performed the analysis. AF contributes data or analysis tools, and MB collected the data, and wrote the paper. All authors reviewed the manuscript.

Funding The authors did not receive support from any organization for the submitted work.

Availability of Data and Materials The data that support the findings of this study are available from the corresponding author upon reasonable request.

Declarations

Conflict of interest The authors declare that they have no conflict of interest.

References

- Zuo, J.; Lin, X.: High-power laser systems. *Laser Photon. Rev.* **16**, 2100741 (2022)
- Li, X.; Yang, X.; Yi, D.; Liu, B.; Zhu, J.; Li, J., et al.: Effects of NbC content on microstructural evolution and mechanical properties of laser cladded Fe50Mn30Co10Cr10-xNbC composite coatings. *Intermetallics* **138**, 107309 (2021)
- Zhang, Z.; Yang, F.; Zhang, H.; Zhang, T.; Wang, H.; Xu, Y., et al.: Influence of CeO₂ addition on forming quality and microstructure of TiC_x-reinforced CrTi₄-based laser cladding composite coating. *Mater. Charact.* **171**, 110732 (2021)
- Rezaei, M.-A.; Naffakh-Moosavy, H.J.J.O.M.P.: The effect of pre-cold treatment on microstructure, weldability and mechanical properties in laser welding of superalloys. *J. Manuf. Process.* **34**, 339–348 (2018)
- Fayazi Khanigi, A.; Farnia, A.; Ardestani, M.; Torkamany, M.J.: Microstructure and mechanical properties of low power pulsed Nd:YAG laser welded S700MC steel. *Sādhanā* **45**, 1–13 (2020)
- Taheri, M.; Halvae, A.; Kashani-Bozorg, S.F.; International, M.: Effect of pre-and post-weld heat treatment on microstructure and mechanical properties of GTD-111 superalloy welds. *Metals Mater. Int.* **27**, 1173–1192 (2021)
- Liang, L.; Xu, M.; Chen, Y.; Zhang, T.; Tong, W.; Liu, H., et al.: Effect of welding thermal treatment on the microstructure and mechanical properties of nickel-based superalloy fabricated by selective laser melting. *Mater. Sci. Eng. A* **819**, 141507 (2021)
- Ameri, M.; Ghaini, F.M.; Torkamany, M.; Technology, L.: Investigation into the efficiency of a fiber laser in surface hardening of ICD-5 tool steel. *Opt. Laser Technol.* **107**, 150–157 (2018)
- Gvozdev, A.; Golyshv, I.; Minayev, I.; Sergeev, A.; Sergeev, N.; Tikhonova, I., et al.: Multiparametric optimization of laser cutting of steel sheets. *Inorg. Mater. Appl. Res.* **6**, 305–310 (2015)
- Ettefagh, A.H.; Wen, H.; Chaichi, A.; Islam, M.I.; Lu, F.; Gartia, M., et al.: Laser surface modifications of Fe-14Cr ferritic alloy for improved corrosion performance. *Surf. Coat. Technol.* **381**, 125194 (2020)
- Farnia, A.; Malek Ghaini, F.; Rao, J.; Ocelík, V.; De Hosson, J.T.M.: Tantalum-modified Stellite 6 thick coatings: microstructure and mechanical performance. *J. Mater. Sci.* **48**, 140–149 (2013)
- Xu, H.; He, T.; Zhong, N.; Zhao, B.; Liu, Z.: Transient thermomechanical analysis of micro cylindrical asperity sliding contact of SnSbCu alloy. *Tribol. Int.* **167**, 107362 (2022)
- Moradi, M.; Arabi, H.; Nasab, S.J.; Benyounis, K.Y.; Technology, L.: A comparative study of laser surface hardening of AISI 410 and 420 martensitic stainless steels by using diode laser. *Opt. Laser Technol.* **111**, 347–357 (2019)
- Dehghani, A.; Torkamany, M.J.: Investigation of the effect of surface transformation hardening by high power diode laser on the microstructure, hardness and wear behavior of AISI O1 cold work tool steel. *Iran. J. Manuf. Eng.* **8**, 14–22 (2021)
- Özerkan, H.B.; Technology: Experimental fatigue life determination of thermo-diffusion surface boronized of AISI 1040 steel. *J. Mech. Sci. Technol.* **33**, 4957–4962 (2019)
- Xuewu, L.; Hongxing, W.; Tian, S.; Chuanwei, Z.; Xiaona, J.; Xuegang, Z., et al.: Efficient preparation and anticorrosion mechanism of superhydrophobic 7075 aviation aluminum alloy. *Rare Metal Mater. Eng.* **51**, 6–10 (2022)
- Telasang, G.; Majumdar, J.D.; Padmanabham, G.; Manna, I.: Wear and corrosion behavior of laser surface engineered AISI H13 hot working tool steel. *Surf. Coat. Technol.* **261**, 69–78 (2015)
- Li, R.; Jin, Y.; Li, Z.; Qi, K.: A comparative study of high-power diode laser and CO₂ laser surface hardening of AISI 1045 steel. *J. Mater. Eng. Perform.* **23**, 3085–3091 (2014)
- Lo, K.; Cheng, F.; Man, H.C.: Laser transformation hardening of AISI 440C martensitic stainless steel for higher cavitation erosion resistance. *Surf. Coat. Technol.* **173**, 96–104 (2003)
- Pinahin, I.; Chernigovskij, V.; Bracihin, A.; Yagmurov, M.: Improvement of wear resistance of VK6, VK8, T5K10, and T15K6 hard alloys by volume pulsed laser hardening. *J. Friction Wear* **36**, 330–333 (2015)
- Sadooghi, A.; Rahmani, K.: Experimental study on mechanical and tribology behaviors of Mg-SiC nano/micro composite produced by friction stir process. *J. Mech. Sci. Technol.* **35**, 1121–1127 (2021)
- Goia, F.A.; de Lima, M.S.F.: Surface hardening of an AISI D6 cold work steel using a fiber laser. *J. ASTM Int.* **8**, 1–9 (2011)
- Martínez, S.; Lamikiz, A.; Taberero, I.; Ukar, E.: Laser hardening process with 2D scanning optics. *Phys. Proc.* **39**, 309–317 (2012)
- Lakhkar, R.S.; Shin, Y.C.; Krane, M.J.M.: Predictive modeling of multi-track laser hardening of AISI 4140 steel. *Mater. Sci. Eng., A* **480**, 209–217 (2008)
- Cordovilla, F.; García-Beltrán, Á.; Sancho, P.; Domínguez, J.; Ruiz-de-Lara, L.; Ocaña, J.L.: Numerical/experimental analysis of the laser surface hardening with overlapped tracks to design the configuration of the process for Cr-Mo steels. *Mater. Des.* **102**, 225–237 (2016)
- Montazeri, M.; Ghaini, F.M.; Ojo, O.: Heat input and the liquation cracking of laser welded IN738LC superalloy. *Weld. J.* **92**, 258s–264s (2013)
- Astm, G.: 99–95a standard test method for wear testing with a pin-on-disk apparatus. *ASTM Int.*, pp. 1–6 (2000)
- Khalid, F.; Farooque, M.; ul Haq, A.; Khan, A.: Role of ferrite/pearlite banded structure and segregation on mechanical properties of microalloyed hot rolled steel. *Mater. Sci. Technol.* **15**, 1209–1215, (1999)
- Xin, T.; Tang, S.; Ji, F.; Cui, L.; He, B.; Lin, X., et al.: Phase transformations in an ultralight BCC Mg alloy during anisothermal ageing. *Acta Mater.* **239**, 118248 (2022)
- Mosavi, A.; Salehi, F.; Náđai, L.; Károly, S.; Gorji, N.E.: Modeling the temperature distribution during laser hardening process. *Res. Phys.* **16**, 102883 (2020)
- Lu, Y.; Ehle, L.C.; Richter, S.; Radel, T.: Influence of multi-pass laser hardening of normalized AISI 4140 on the grain size. *Surf. Coat. Technol.* **421**, 127434 (2021)
- Muthukumaran, G.; Dinesh Babu, P.: Laser transformation hardening of various steel grades using different laser types. *J. Braz. Soc. Mech. Sci. Eng.* **43**, 1–29 (2021)
- Babu, P.D.; Buvanashakaran, G.; Balasubramanian, K.R.: Experimental studies on the microstructure and hardness of laser transformation hardening of low alloy steel. *Trans. Can. Soc. Mech. Eng.* **36**, 241–258 (2012)
- Selvan, J.S.; Subramanian, K.; Nath, A.: Effect of laser surface hardening on En18 (AISI 5135) steel. *J. Mater. Process. Technol.* **91**, 29–36 (1999)
- Komanduri, R.; Hou, Z.: Thermal analysis of laser surface transformation hardening—optimization of process parameters. *Int. J. Mach. Tools Manuf.* **44**, 991–1008 (2004)
- El-Batahy, A.-M.; Ramadan, R.A.; Moussa, A.-R.: Laser surface hardening of tool steels—experimental and numerical analysis. *J. Surf. Eng. Mater. Adv. Technol.* (2013)
- Allmen, M.V.; Blatter, A.: Laser-beam interactions with materials: physical principles and applications vol. 2: Springer Science & Business Media (2013)



38. Putatunda, S.; Nambiar, M.; Clark, N.: Influence of laser hardening on mechanical properties of a low alloy steel. *Surf. Eng.* **13**, 407–414 (1997)
39. Babu, P.D.; Balasubramanian, K.; Buvanashakaran, G.: Laser surface hardening: a review. *Int. J. Surf. Sci. Eng.* **5**, 131–151 (2011)
40. Grum, J.J.H.O.R.S.; Steel, D.O.: Induction hardening. *ASM Int.* **2**, 220–247 (2002)
41. Casalino, G.; Moradi, M.; Moghadam, M.K.; Khorram, A.; Perulli, P.: Experimental and numerical study of AISI 4130 steel surface hardening by pulsed Nd: YAG laser. *Materials* **12**, 3136 (2019)
42. A. Nath and S. Sarkar, *Laser transformation hardening of steel*, in *Advances in laser materials processing*, ed: Elsevier, 2018, pp. 257–298.
43. Sadooghi, A.; Rahmani, K.; Hashemi, S.: Effects of Nano and Micro size of MgO on mechanical properties, wear, and corrosion of magnesium matrix composite. *Strength Mater.* **53**, 983–997 (2021)

Springer Nature or its licensor (e.g. a society or other partner) holds exclusive rights to this article under a publishing agreement with the author(s) or other rightsholder(s); author self-archiving of the accepted manuscript version of this article is solely governed by the terms of such publishing agreement and applicable law.